ADVANCED MATERIALS
www.advmat.de

Decoupling and Reprogramming the Wiggling Motion of Midge Larvae Using a Soft Robotic Platform

Neng Xia, Bowen Jin, Dongdong Jin, Zhengxin Yang, Chengfeng Pan, Qianqian Wang, Fengtong Ji, Veronica Iacovacci, Carmel Majidi, Yang Ding,* and Li Zhang**

The efficient motility of invertebrates helps them survive under evolutionary pressures. Reconstructing the locomotion of invertebrates and decoupling the influence of individual basic motion are crucial for understanding their underlying mechanisms, which, however, generally remain a challenge due to the complexity of locomotion gaits. Herein, a magnetic soft robot to reproduce midge larva's key natural swimming gaits is developed, and the coupling effect between body curling and rotation on motility is investigated. Through the authors' systematically decoupling studies using programmed magnetic field inputs, the soft robot (named LarvaBot) experiences various coupled gaits, including biomimetic side-to-side flexures, and unveils that the optimal rotation amplitude and the synchronization of curling and rotation greatly enhance its motility. The LarvaBot achieves fast locomotion and upstream capability at the moderate Reynolds number regime. The soft robotics-based platform provides new insight to decouple complex biological locomotion, and design programmed swimming gaits for the fast locomotion of soft-bodied swimmers.

1. Introduction

Natural organisms often exhibit high adaptability to complex environments due to the evolution of predator-prey interactions, such as ultrafast locomotion, camouflage, and group cooperation.[1–3] Studies on natural motion and adaptation have significant influence on various engineering fields, ranging from bioinspired robotics to medical devices.[4–10] However, given the complexity of biological behaviors, emulating and investigating these natural modes of locomotion with engineered systems has been challenging.[11–13] In this respect, burgeoning effort has been devoted to developing new simulation tools, physical models, and experimental platforms. Among these engineering tools, soft robotic systems are promising in light of their biologically relevant mechanical compliance, deformability, and modes of locomotion.[4,14–17]

Untethered soft robots, which can freely move without requiring a physical connection to external hardware and power supplies, are good candidates for studying the locomotion modes of natural invertebrates.[18–21] Thanks to recent advances in fabrication methods,[22–26] functional materials,[27–29] and actuation strategies,[7,30–35] roboticists have proposed several soft robots that are capable of mimicking some features of natural animal locomotion. For example, previous efforts with photo-responsive hydrogels-based robots demonstrated the ability to mimic peristaltic earthworm crawling.[36] Likewise, untethered soft robots powered with shape memory alloy have been shown to exhibit a variety of locomotion modes, including undulation, jumping, crawling through narrow space or walking over rough terrain.[37,38] The application of magnetic soft robots in biomimetic study has received growing attention due to their high controllability. Hu et al. developed a millimeter-scale film robot that achieves multiple locomotion modes,

---

N. Xia, D. Jin, Z. Yang, C. Pan, Q. Wang, F. Ji, V. Iacovacci, L. Zhang
Department of Mechanical and Automation Engineering
The Chinese University of Hong Kong
Hong Kong SAR 999077, China
E-mail: lizhang@cuhk.edu.hk

B. Jin, Y. Ding
Beijing Computational Science Research Center
Haidian District, Beijing 100193, China
E-mail: dingyang@csrc.ac.cn

V. Iacovacci
The BioRobotics Institute
Scuola Superiore Sant'Anna
Pisa 56025, Italy

C. Majidi
Soft Machines Lab
Carnegie Mellon University
Pittsburgh, PA 15213, USA
E-mail: cmajidi@andrew.cmu.edu

L. Zhang
Chow Yuk Ho Technology Center for Innovative Medicine
The Chinese University of Hong Kong
Hong Kong SAR 999077, China

L. Zhang
CUHK T Stone Robotics Institute
The Chinese University of Hong Kong
Hong Kong SAR 999077, China

L. Zhang
Department of Surgery
The Chinese University of Hong Kong
Hong Kong SAR 999077, China

The ORCID identification number(s) for the author(s) of this article can be found under https://doi.org/10.1002/adma.202109126.

DOI: 10.1002/adma.202109126

e.g., jellyfish-like swimming and crawling.[5] Recently, soft magnetic composites with programmable 3D magnetization and smart materials have been further developed to realize diverse biomimetic motorial capabilities.[16,22,39,40] However, despite such progress, many organisms at different scales exhibit more complex locomotion gaits that have been difficult to mimic with existing soft robotic platforms, and these platforms suffer from the lack of a strategy to decouple the complex biological behaviors. This makes it challenging to reconstruct their locomotion behaviors or to understand the underlying mechanisms of the different locomotion modes. For example, midge larvae (Chironomidae), swim rapidly (Reynolds number $Re \approx 465$) with a unique gait consisting of periodically curling into a circle shape coupled with body rotation and unfolding driven by muscle activation.[41] The larvae yield faster swimming speed with a unique coupled gait (0.84 body length per motion cycle) compared with many other invertebrates (including nematode,[42] polychaete worm,[43] leech,[44] caterpillar,[45] and earthworm[46]) (Table S1, Supporting Information) and exhibit high adaptability to complex environments.[41] In addition, compared with undulatory swimming adopted by sperm cells and zebrafish (0.09–0.51 body length cycle^{-1}),[47] the wiggling motion also has the benefit of enabling fast swimming speed at moderate *Re* regime. Walking and crawling represent additional modes of locomotion that are commonly utilized by many organisms and serve as a relatively robust way to move over solid surfaces. However, such locomotion is typically friction-controlled and requires sufficient traction with contacting surfaces in order to achieve controlled motion. Therefore, the study of the wiggling motion of midge larvae promises benefits in constructing soft aquatic robots with high mobility and adaptability, which is attractive to researchers.

In this work, we present a millimeter-scale magnetic soft robot (named LarvaBot) that reconstructs the natural swimming gait of midge larvae and provides a platform to understand their agile locomotion that could potentially guide actuation, gait selection, and path planning of other untethered swimming robots. The motion cycle of natural larvae is divided into two stages, and each of them consists of three types of gaits, including unfurling, curling, and rotation (**Figure 1**A). LarvaBot is designed to achieve similar motion through the use of a shape programmable composite composed of soft hydrogel material doped with ferromagnetic particles with anisotropic magnetization. Taking advantage of photocurable hydrogel, we can facilely fabricate our soft robot (curing time less than 5 min) with a slender structure. Inspired by the morphology of midge larvae, we adopt a rod-shape structure which is different from the film-shape magnetic robots. New time-varying magnetic fields are introduced to induce the agile motion of our LarvaBot. A variety of reprogrammable coupled gaits, including the characteristic larvae ones, are created through our LarvaBot and programmed magnetic field inputs (Figure 1B). By performing systematical decoupling studies, we unveil that the coupling of body curling and rotation plays a key role in its propulsion. In fact, we discover that an optimal rotation amplitude and the synchronization of curling and rotation greatly enhance motility. Swimming with this biomimetic propulsion fashion can induce ring vortex structures consistent with the natural counterpart and achieve great motility (0.71 body length per motion cycle) at moderate Re regimes (1–2000).[48] Moreover, LarvaBot is capable of performing upstream locomotion in flowing fluid, adaptability to a 3D environment by switching its locomotion modes, and other functionalities, including obstacle-crossing ability and movement in narrow space. Compared with the magnetic force control strategy, which directly drives the robot to a prescribed position via the magnetic field gradient, the LavarBot allows for dexterous control in its ability to achieve prescribed modes of deformation and motion. This work provides a soft robotic platform allowing to decouple and reprogram the complex wiggling motion adopted by invertebrates and to grasp their underlying mechanisms. It also offers new insight for designing optimized swimming soft robots with complex coupled gaits which may outperform their natural counterparts.

2. Results and Discussion

2.1. Morphology and Swimming Gait of Midge Larvae

Chironomidae midge larvae, a kind of soft-bodied insect living in ponds, exhibit unique locomotion behavior.[41] Figure 1A illustrates a complete motion cycle and shape of the larvae. With a body length ranging from 2.0 to 29.4 mm, the larva consists of an anterior head, a slender body, and a posterior proleg.[41,49–51] The complex swimming gait of larva in the horizontal plane can be divided into two stages. At the beginning of the first half stroke, the larva's body flexes to one side forming a circle-like structure, followed by body rotation and rapid unfurling. The larva body rotates ≈180° after half-strokes. At the second stage, the larva coils to the other side, rotates along the opposite direction, and eventually points in almost the same direction as at the start.[41,52] An S-shaped trajectory can be obtained during one motion cycle and the direction of effective displacement generated by the asymmetric motion sequence is perpendicular to the larva body in the unfurling configuration. With the complex coupling of curling and rotation, the larvae can exhibit highly maneuverable swimming behavior that enables them to escape from many natural predators. Apart from fast swimming, multimodal locomotion including crawling, undulation, emersion, and immersion have been observed in larvae.[41] This abundance of modalities in motile activity enables them to adapt to sophisticated physical environmental circumstances.

2.2. Reconstruction of the Biomimetic Locomotion

The LarvaBot is inspired by the morphology and kinematic characteristics of the natural larvae. Our LarvaBot exhibits slender structure and deformation to arc shape under external magnetic field. The comparison between the larvae and the LarvaBot is shown in **Table 1**. Considering the workspace of the actuation setup and the morphological characteristics of the real larvae, the LarvaBot is designed as a slender rod structure whose length and aspect ratio are 5 mm and 11:1, respectively. The LarvaBot swims in an intermediate flow regime and the induced wake flow pattern is consistent with the midge larvae (Re = 17–57). The difference in characteristic length of LarvaBot and collected larvae in reference[41] can lead to the difference in *Re* number. In this study, the robot body is composed of

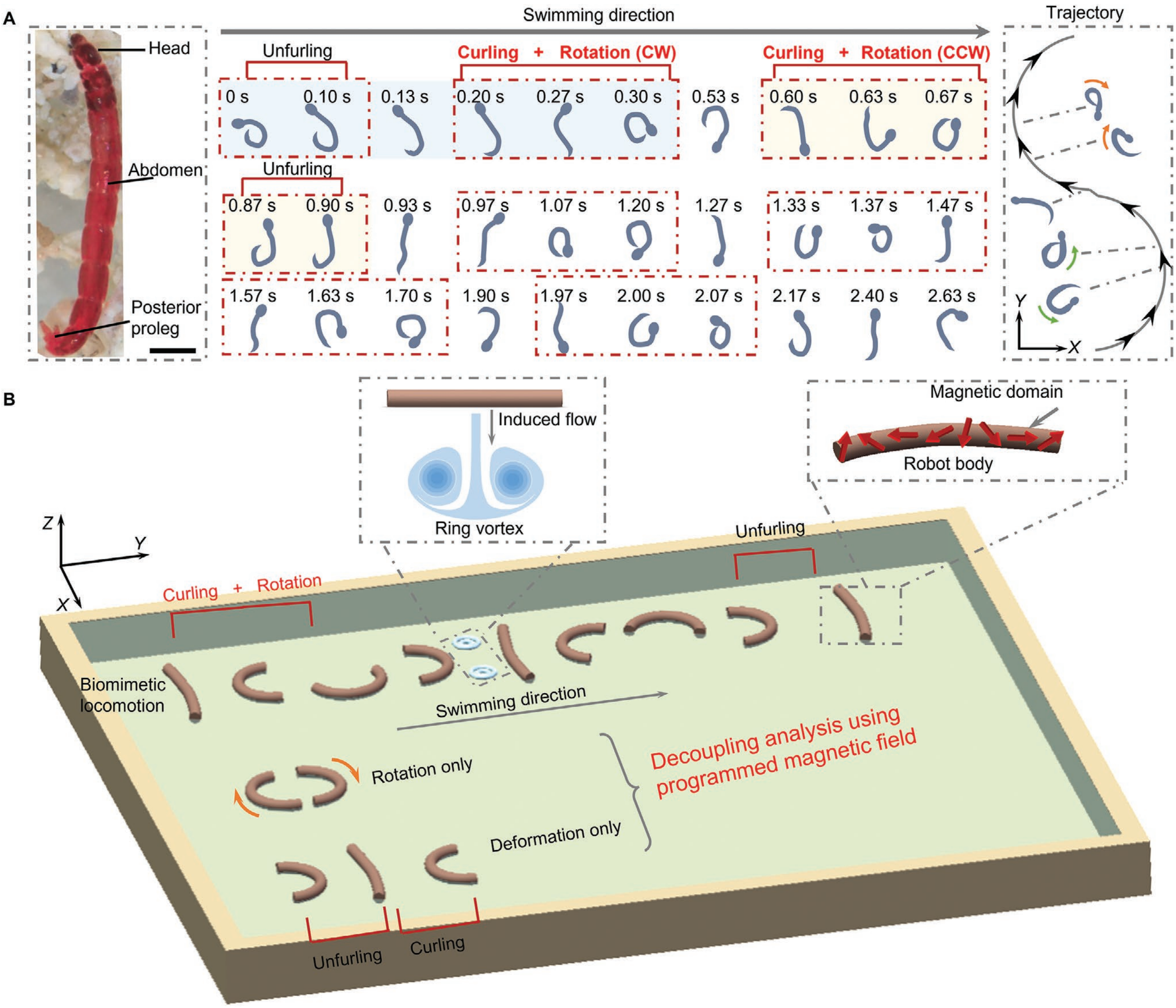

Figure 1. Schematics of the larvae and LarvaBot locomotion. A) Image and swimming behavior of midge larva in the horizontal plane. Red boxes indicate critical postures of the larva. The motion of larva can be divided into two stages, each consisting of unfurling and coupled curling and rotation. Larva coils to different sides in the two stages. CW and CCW represent clockwise and counterclockwise rotation, respectively. A schematic diagram of the trajectory of larva is shown on the right side of the graph. An S-shaped trajectory is generated during the swimming behavior and the inset images of larva show their orientations. The photo of the larva is reproduced with permission.[51] Copyright 2015 , The Zoological Society of Japan. The gaits are extracted from the motion of real midge larvae. The scale bar is 1 mm. B) Schematics of the LarvaBot with a variety of reprogrammable coupled gaits, including the biomimetic swimming gait and the decoupling of basic motion. The basic gaits of the robot include curling, unfurling, and rotation, which are activated by a time-varying magnetic field. A ring vortex structure is generated by the propulsion of the LarvaBot and consistent with the wake structure created by the larvae.

polyacrylamide (PAAm) hydrogel and hard magnetic NdFeB@SiO_2 particles (remanent magnetic moment: 85 emu g^{-1}, Figure S1, Supporting Information) with an average diameter of 5 µm (Figure S2, Supporting Information, and **Figure** 2A). To avoid the influence of the solid substrate (such as surface friction) on the robot's motion, hydrophobic treatment is conducted on the surface of the robot to enable stable locomotion at the air–water interface. Surface tension analysis in Section S1 (Supporting Information) demonstrates that the surface tension applied to the LarvaBot does not affect its locomotion. The shape transformation is controlled by the interaction between the magnetization of the robot and the programmed magnetic field. As shown in Figure 2A and Figure S3 (Supporting Information), a template-assisted magnetization method is adopted to obtain a sinusoidal magnetization profile [$M = (m_x, m_y, 0)$] inside the robot body. The magnetic flux density created by the magnetization profile of the LarvaBot is measured by a magneto-optical sensor (MagViewS, Matesy, Germany), as shown in Figure 2B. A simulation for the sinusoidal magnetization profile is also developed in COMSOL (Figure 2B). The agreement between the simulation and measured results of surface magnetic flux density verifies the sinusoidal distribution of the magnetization profile.

Table 1. Comparison between LarvaBot and midge larvae.

Aspects of comparison		Midge larvae	LarvaBot
Morphology	Length [mm]	2.0–29.4[41,49]	5
	Aspect ratio	10.4–14.3[50,52]	11
	Geometry	Cylindrical body	Uniform, cylindrical shape
Kinematics and dynamics	Flow regime	Intermediate flow regime ($Re = 350, 465$)[41,52]	Intermediate flow regime ($Re = 17–57$)
	Actuation frequency [Hz]	2.66[41]	1–4
	Motility [BL cycle^{-1}]	0.84[41]	0.04–0.71
	Actuation method	Muscle[41]	Magnetic torque
	Wake flow pattern	Ring vortex[52]	Ring vortex
	Swimming plane	Horizontal plane[41]	Horizontal plane

The LarvaBot deforms into arc shapes with different curvatures and orientations by applying static magnetic fields, as shown in Figure 2C and Figure S4 (Supporting Information). A three-axis Helmholtz electromagnetic coil setup is used to generate the magnetic field (Figure S5, Supporting Information). The curvature of the deformed robot increases as the strength of the magnetic field increases. The deformation of the LarvaBot can be quantitatively described by the following elastic rod model[5]

$$\left(m_x sin\theta + m_y cos\theta\right) B_x - \left(m_x cos\theta - m_y sin\theta\right) B_y = \frac{EI}{A}\frac{\partial^2\theta}{\partial s^2} \tag{1}$$

Here, E and θ represent the elastic modulus and the rotational deflection of the robot, respectively, I is the second moment of area of the robot, and A is the cross-sectional area of the robot. $\boldsymbol{B} = \begin{bmatrix} B_x & B_y & B_z \end{bmatrix}^T$ represents the applied magnetic field. The calculated deformation results are in good agreement with the experimental results (Figure 2C). The LarvaBot has a net magnetic moment M_{net} at rest and deformed states, which can be obtained by

$$\boldsymbol{M}_{net} = \int_L \boldsymbol{R}_z \boldsymbol{M} \, Ads \tag{2}$$

where L is the body length of the robot and Rz is a z-axis rotational matrix regarding the change in the direction of M. As shown in Figure 2C, the robot's M_{net} tends to be aligned with B. When the direction of B changes suddenly, the LarvaBot undergoes rigid-body rotation or deformation depending on the magnitude of the change in the direction of B (Figure S6, Supporting Information). When the angle exceeds 90°, the robot will be deformed until the M_{net} aligns with the direction of B. In contrast, if the angle is less than 90°, a rigid-body rotation occurs. In addition, the LarvaBot could achieve S-shaped deformation with the programmable magnetic fields and the interaction between the robot body and surrounding boundaries, as shown in Figure S7 (Supporting Information).

Based on the magnetic responsive behaviors of the robot under static magnetic fields, a dynamic programmed magnetic field (Section S2, Supporting Information) is designed to generate the larva-inspired swimming gait. We divide it into two parts to show the applied magnetic field more clearly, as shown in Figure 2D. During the first half period, the magnetic field rotates with increasing strength until the magnitude reaches its maximum, and then it gradually decreases to 0 at a constant angle. During the second phase, the strength of the magnetic field changes with the same trend, but the magnetic field rotates in the opposite direction. The motion sequences of the LarvaBot induced by the proposed dynamic field are shown in Figure 2E. During the CCW rotation period, the LarvaBot curls into arc shape and experiences rotation due to magnetic torque. At the end of the CCW rotation period, the robot body unfurls and points to the opposite direction compared with the initial orientation. Subsequently, the LarvaBot bends toward the other side and recoveries the same head-to-tail direction as at the beginning of the CW period. The motion sequences of the LarvaBot are consistent with the swimming gait of larvae shown in Figure 1A. The net displacement over one cycle and swimming direction can be determined by the initial and final states of the LarvaBot. The swimming direction in Figure 2E is approximately perpendicular to the robot's body at straightened state. These results indicate that the proposed robot exhibits a consistent directional movement by emulating the swimming gait of larvae.

2.3. Swimming Mechanism of the LarvaBot

The movement of the LarvaBot could be simplified into two key processes: unfurling of the robot body (unfurling process) and body rotation coupled with curling (C-R process). Figure S8 (Supporting Information) illustrates the variation of curvature and rotation angle of the LarvaBot during one motion cycle. The instantaneous velocity of the center of mass (COM) of the robot is shown in **Figure 3**A. The positive displacement mainly occurs during the C-R process (blue regions in Figure 3A). According to the movement trajectories extracted from experimental results, the rotation of the COM of the robot is observed. On the other hand, during the unfurling process, M_{net} aligns with the external magnetic field. However, no net magnetic torque and magnetic force act on the robot. Fluid dynamic simulation demonstrated that the fluid force acting on the robot is negligible. Therefore, the COM of the robot hardly changes (Figure S9, Supporting Information). Based on the above analysis, the average velocity of the robot over one cycle could be calculated as

$$v = L_{\mathrm{C-R}} \times f_{eq} = \frac{L_{\mathrm{C-R}}}{\frac{1}{2f_1}\left(1 + \frac{f_1}{f_2}\right)} \tag{3}$$

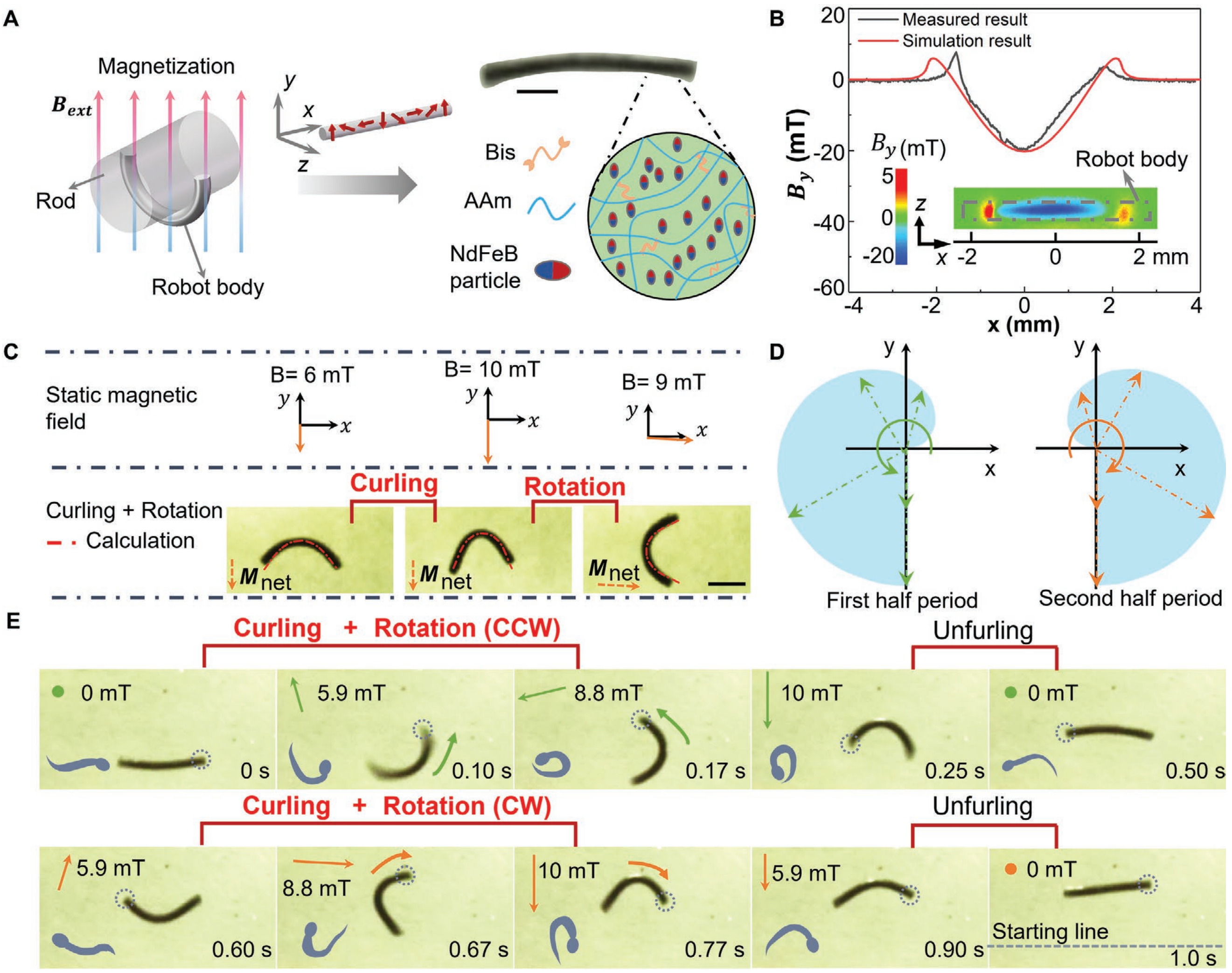

Figure 2. Magnetic control and motion analysis of the LarvaBot. A) Magnetization of the robot. The scale bar is 1 mm. B) Simulation and measured results of magnetic flux density distribution (B_y) along the centerline of the LarvaBot. The inset shows magnetic flux density distribution at the robot surface measured by a magneto-optical sensor. C) Deformation and orientation of the LarvaBot under different static magnetic fields. The scale bar is 2 mm. D) Magnetic field used to control the swimming behavior of LarvaBot. The straight arrows represent the time-varying magnetic field. The magnetic field rotates clockwise (CW) and counterclockwise (CCW) represented by the green and orange colors, respectively. During the first half period, the magnetic field rotates with increasing strength until the magnitude reaches its maximum, and then it gradually decreases to 0 at a constant angle. During the second period, the strength of the magnetic field changes in the same trend, but the magnetic field rotates in the opposite direction. E) Motion sequence of the LarvaBot in one cycle. The scale bar is 2 mm. The dashed circles indicate the "head" of the robot and distinguish the orientation of the robot body at different times.

where $1/f_1$ and $1/f_2$ represent the duration of the C-R and unfurling process, respectively. f_{eq} is the frequency for one motion cycle. We define the net displacement generated during the C-R process as L_{C-R}.

Theoretical analysis is performed to study the fluid-structure interaction during the swimming process. We use a sine function to describe the variation of curvature of the robot body during one motion cycle. By performing computational fluid dynamic simulation with immersed boundary method (Section S3, Supporting Information), the LarvaBot COM trajectory and the fluid-structure interaction can be derived. Figure 3B shows the comparison between experimental and simulation results, in which the trajectory and shape of the robot over one cycle are included. The agreement between the experimental and simulation results validates the simulation model. The S-shaped trajectory is repeatable after many cycles of motion, as shown in Figure S10 (Supporting Information). The net fluid force acting on the LarvaBot is shown in Figure 3C. The net fluid force increases dramatically during the C-R process and becomes negligible during the unfurling process. This behavior is in line with the no net displacement of the LarvaBot COM during unfurling. We also demonstrate that different types of robots such as a cuboid-shaped robot with segmented structure can also adopt this locomotion mechanism, as shown in Figure S11 (Supporting Information). The robot body is composed of magnetic section (fabricated by polyacrylamide hydrogel doped with magnetic particles) and nonmagnetic section (fabricated by polyacrylamide hydrogel). The robot structure is obtained

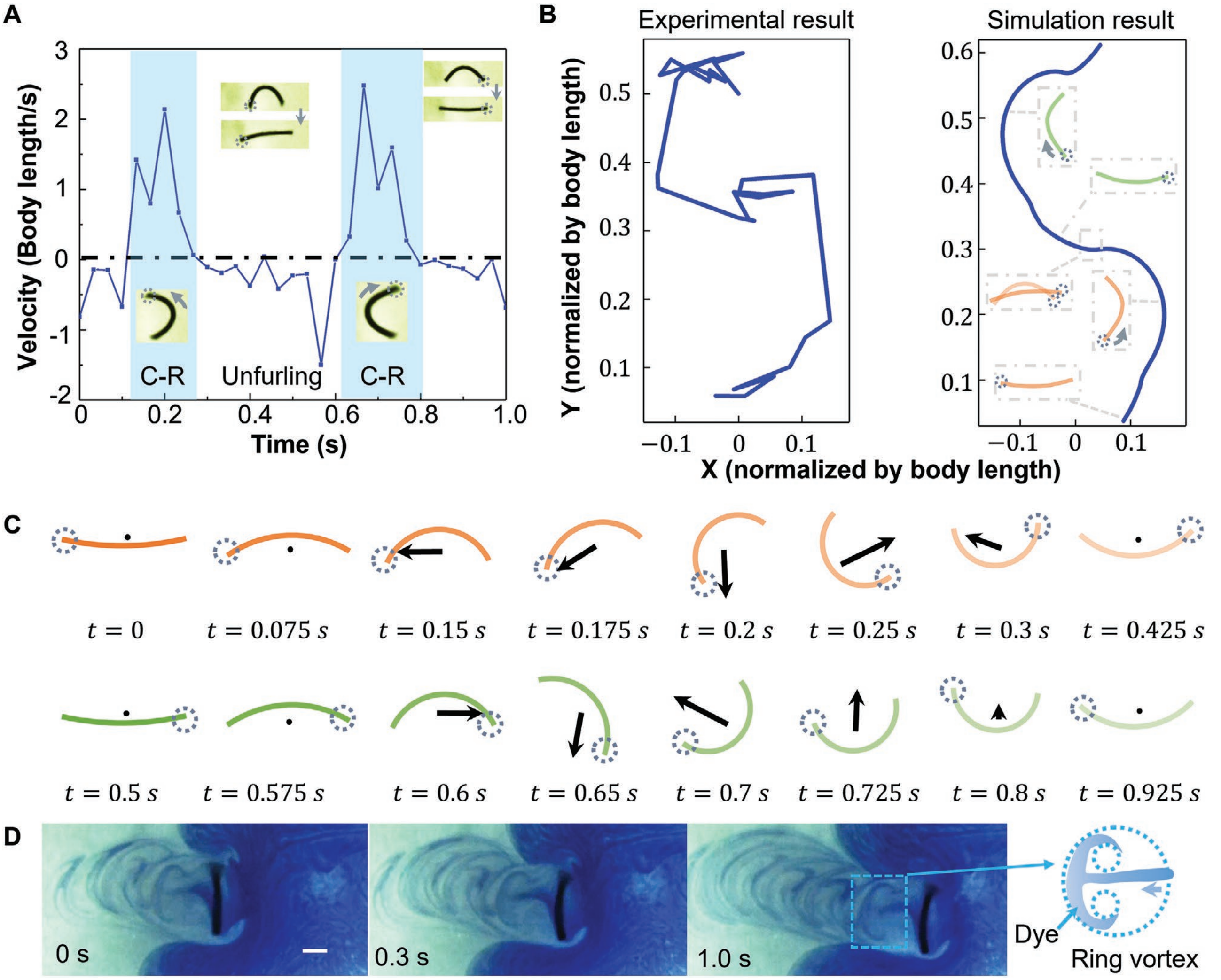

Figure 3. Fluid dynamic simulation and visualization of wake structure. A) Measured instantaneous velocity of the LarvaBot in one cycle. The inset images show the robot during the unfurling process and C-R process. B) Experimental and simulation results for the trajectory of the center of mass (COM) of the LarvaBot. The inset schematics show the orientation of the robot at different positions. The displacement of the robot in *X* and *Y* direction is normalized by its body length. C) Net fluid force applied to the robot body over one motion cycle. Green and orange curves represent the orientation of the robot at different times, and black arrows represent the direction and amplitude of net fluid force. D) Wake structure visualized by dye and geometry of ring vortex. The scale bar is 2 mm.

by a 3D printer (NanoArch S130, BMF Precision, China). With the same magnetization method and magnetic field inputs shown in Figure 2, the robot could also complete the biomimetic swimming gaits and generate net displacement over one motion cycle.

In addition, the impact of the biomimetic swimming gait on the flow field is studied. The wake structure created by the swimming gait is visualized using organic dye, as shown in Figure 3D and Movie S1 (Supporting Information). As a result of motion generated by LarvaBot, an array of ring vortexes consisting of two counterrotating vortex cores is generated behind the robot, demonstrating that the propulsive force is derived by accelerating water into the wake structure. The vortex pattern is consistent with that induced by the motion of the larvae,[52] which further verifies the biomimetic feature of the LarvaBot. The propulsion force is calculated to be 0.4 μN and the details of the propulsion force calculation can be found in Section S4, Figures S12 and S13 (Supporting Information).[53]

2.4. Further Understanding the Complex Coupled Wiggling Motion Using Larvabot

Our LarvaBot-based platform provides an enabling robotic technology to decouple the influence of various kinematic parameters that significantly affect their swimming performance. To provide a more accurate comparison of performance, we use the normalized velocity (v/fL, where v is the velocity of the robot, f is actuation frequency, L is the body length of the robot) to evaluate the motility of our LarvaBot.[54] First, we study the coupling of the body curling and rotation by tuning the phase difference of these basic motions. The impact of the phase

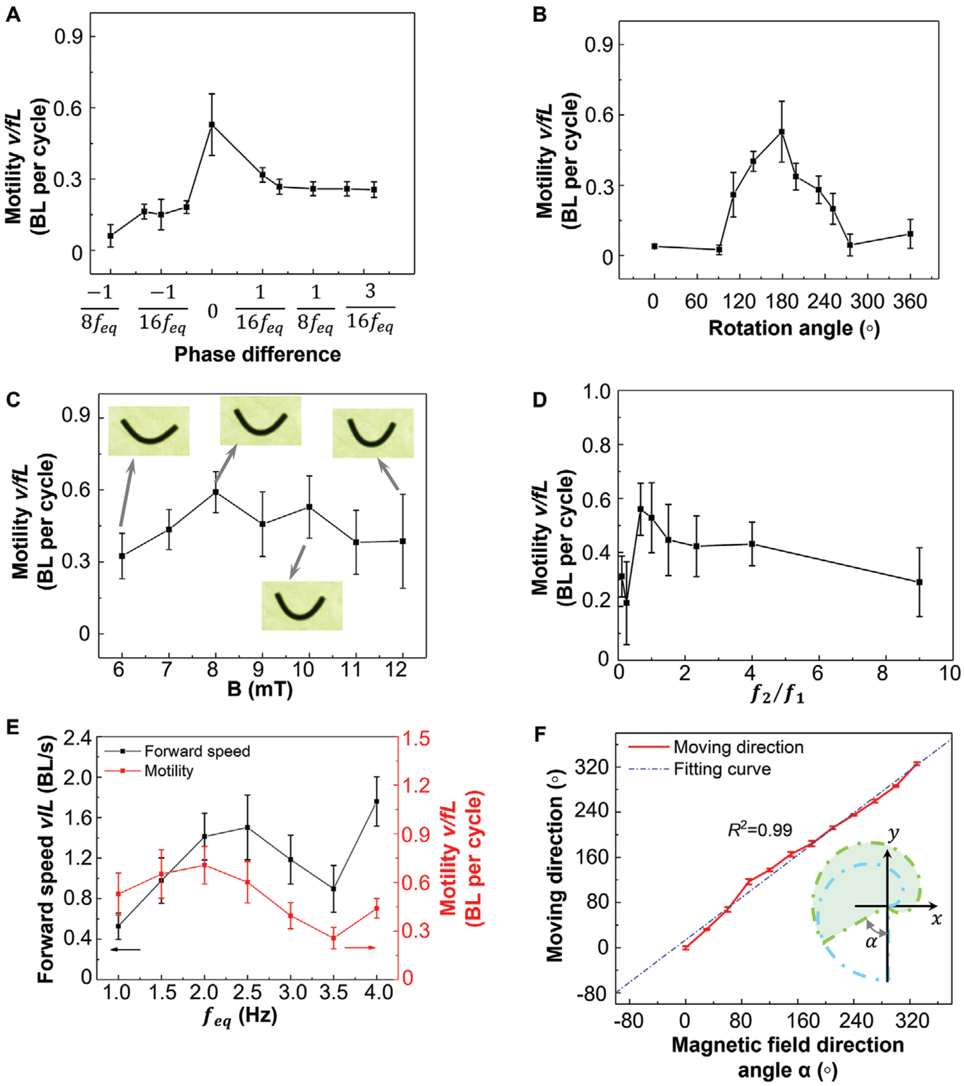

Figure 4. LarvaBot-based platform for decoupling the complex wiggling motion. A) Effect of the phase difference between curling and rotation on motility. The minus value represents that there is a phase lag of rotation compared with the curling process. BL represents body length of the LarvaBot. B) Effect of the rotation angle of robot body over half cycle on the motility. C) Effect of magnetic field strength on the motility of the LarvaBot. Inset images show the deformation of the LarvaBot under B = 6, 8, 10, and 12 mT. D) Effect of f_2/f_1 on the motility of the LarvaBot. E) Effect of f_{eq} on the motility and forward velocity (BL s^{-1}) of the LarvaBot. F) Relationship between the moving direction and the direction angle of the magnetic field. The inset image shows the definition of the direction angle of the magnetic field. To describe the moving direction of the LarvaBot, we use the swimming direction of the robot under the direction angle of 0° as a baseline for comparison. Error bars represent the standard error of the mean and the number of trials $n = 6$.

difference between curling and rotation on the motility and trajectory of the robot is shown in **Figure** 4A, Figure S14 and Movie S2 (Supporting Information), where a minus value for phase difference means that there is a delay of the rotation compared with the curling process. Experimental results illustrate that S-shaped trajectories are obtained under different phase differences. Moreover, the results show that performing the curling and rotation synchronously can yield the largest net displacement over one motion cycle rising to 769% when reaching the maximum. Furthermore, the impact of basic motion parameters (e.g., rotation amplitude, rotational speed, and deformation amplitude) on motility is investigated through the decoupling study on LarvaBot. As aforementioned, both LarvaBot and larvae rotate 180° after half-strokes. Different rotation angles ranging from 0° to 360° are achieved by tuning the input magnetic field parameters. The 0° rotation angle indicates that the robot only experiences curling and unfurling. Figure 4B and Figure S15 (Supporting Information) show that the motility (v/fL) of LarvaBot attains its maximum at 180° rotation with a rise of 1245%. This confirms that the optimal ability of the proposed microrobot is consistent with the biological larva behavior reported in previous work.[41] In addition, we analyzed the variation of deformation amplitude by tuning the magnetic field strength. With the increase of the magnitude of B, the curvature of the deformed robot also increases (Figure S16, Supporting Information), and the results show a rise by 82% in motility when reaching the peak velocity (Figure 4C). The fluctuation amplitude of the motility caused by the change of the magnetic field strength is smaller than those caused by the variation of phase difference and rotation amplitude.

The impacts of the duration of C-R (curling and rotation) and unfurling processes are studied through the variations of their relative frequencies f_2/f_1 and total frequency f_{eq} of the full motion cycle. Figure 4D shows the effect of f_2/f_1 on motility (when fixing $f_{eq} = 1$ Hz). The normalized velocity v/fL reaches its maximum when $f_2/f_1 = 0.67$, which indicates the propulsion efficiency benefits from comparable C-R and unfurling processes duration. Furthermore, f_{eq} also has an effect on the motility, as shown in Figure 4E (where f_2/f_1 is fixed at 1). v/fL reaches its maximum (0.71 body length cycle^{-1}) when f_{eq} increases up to 2 Hz and drops to 0.26 body length cycle^{-1} at $f_{eq} = 3.5$ Hz. This demonstrates that the performance of the LarvaBot also relies on its actuation frequency.

LarvaBot is capable of executing a natural swimming gait with controllable propulsion that is optimized for speed. As shown in Figure 4F, there is a linear relationship between the moving direction of the LarvaBot and the direction angle of the magnetic field ($R^2 = 0.99$). The actuation of the LarvaBot does not exhibit noticeable performance deterioration upon long-time exposure to the magnetic field (Figure S17, Supporting Information). When using optimized magnetic field parameters, LarvaBot outperforms most reported robots at moderate *Re* regime in terms of motility/body weight ratio (**Figure 5**).[5,41,47,55–58] Compared with the film robot with jellyfish-like swimming,[5] the LarvaBot breaks time-reversal symmetry and generates an S-shaped trajectory (Figure 3B) within one motion cycle. With a weight of only 0.797 mg, the LarvaBot owns fast forward speed (0.71 body length cycle^{-1}). Nevertheless, LarvaBot velocity is still lower than the biological counterpart[41] (0.84 body length cycle^{-1} at 2.66 Hz). The discrepancy of motility between the proposed LarvaBot and larvae can be attributed to the difference in surface friction caused by the fabrication method.

2.5. Multimodal Locomotion of the LarvaBot

Controllability and robustness are potentially important features in the design and operation of soft robots. Taking advantage of the larva-inspired swimming gait, we demonstrate a trajectory control for the LarvaBot, as shown in **Figure 6**A and Movie S3 (Supporting Information). The LarvaBot could complete a pentagram-shaped trajectory by tuning the direction angle of the magnetic field, which demonstrates the controllability of the swimming gait. Furthermore, the robustness of the LarvaBot is verified in the flowing condition generated by a peristaltic pump. As shown in Figure 6B and Movie S4 (Supporting Information), the robot is passively carried by the flowing fluid with an average speed of 5.5 mm s^{-1} when the magnetic field is off. By applying the magnetic field in Figure 2D ($f_{eq} = 3$ Hz), the LarvaBot could swim against the drag force of the flowing water.

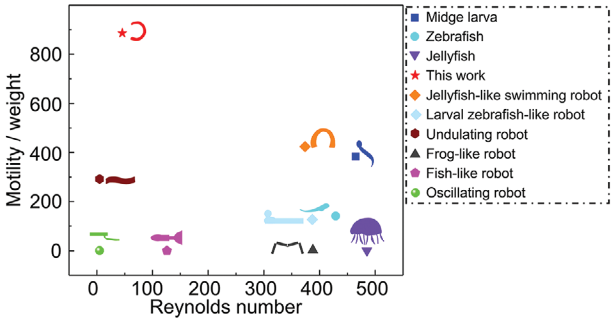

Figure 5. Comparison between LarvaBot, other swimming soft robots and invertebrates at moderate *Re* regime presented in the literature. Other swimming soft robots include jellyfish-like swimming robot,[5] undulating robot,[55] larval zebrafish-like robot,[16] frog-like robot,[56] and oscillating robot,[57] and organisms include midge larvae[41,58] and zebrafish.[47]

Apart from the swimming gait mentioned above, the larvae also show multimodal locomotion to accommodate various physical environmental circumstances and in response to threats. The transformable locomotion modes are achieved by different patterns of muscle activation. Inspired by these behaviors of larvae, various time-varying magnetic fields are designed to generate series of locomotion modes. As shown in Figure 6C, the LarvaBot swims along a 3D trajectory by tuning the pitch angle of the magnetic field (Section S2 and Figure S18, Supporting Information). To demonstrate the controllability of the 3D swimming behavior, the LarvaBot is manipulated to pass through a ring-shaped obstacle back and forth many times (Movie S5, Supporting Information). In addition, the slender body of the robot enables it to go through a small size tube easily. As shown in Figure 6D and Movie S6 (Supporting Information), thanks to the precise control using the applied magnetic field, the robot can enter a tube with a 1.8 mm inner diameter from an open environment and move crawl inside the tube. Untethered robots that could move in a narrow space have broad application prospects, such as executing detection in harsh environments and carrying drugs for treatment in blood vessels. Unlike film-shaped robots, the proposed slender robot with circular cross section exhibits more flexible motion and suffers from fewer space restrictions, making it more suitable for accomplishing tasks in narrow spaces.

Furthermore, a sequential series of locomotion modes can be performed by the LarvaBot to allow it to move in 3D space. As shown in Figure 6E and Movie S7 (Supporting Information), the LarvaBot initially swims at the air–water interface with the bioinspired swimming gait. Just as natural larvae can escape from a liquid surface when they receive external stimuli, our robot can also emerge from water and quickly climb a stair by rolling. To enable the underwater locomotion of the LarvaBot, a transition magnetic field is applied, as shown in Figure S19 and Section S2 (Supporting Information). In this case, we set the pitch angle of the magnetic field as 90° and the rotating plane of the magnetic field is perpendicular to the air-water interface. The deformation and motion of the LarvaBot are completed at the vertical plane which could reduce the body contact with the liquid surface. Since the robot is denser than the water, the LarvaBot could leave the liquid surface and immerse in the liquid environment to complete the underwater locomotion shown in Figure 6. Subsequently, the LarvaBot swims over a standing obstacle as high as 8 mm (1.6 body length), demonstrating its obstacle crossing ability. Figure S20 and Movie S8 (Supporting Information) summarize seven different locomotion modes

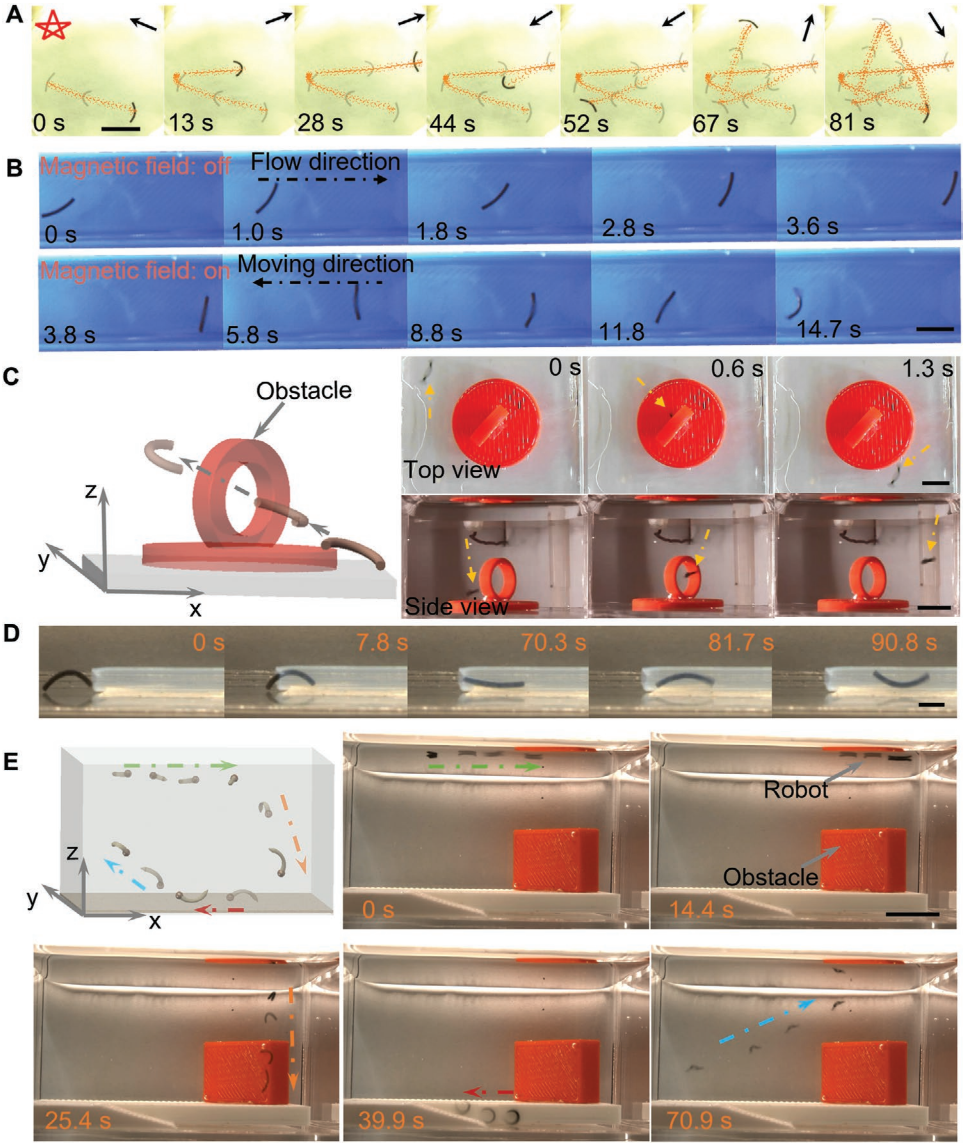

Figure 6. Multimodal locomotion of the LarvaBot. A) Controllable movement of the LarvaBot along a pentagram trajectory. Arrows show the moving direction. The scale bar is 10 mm. B) Propulsion of the LarvaBot in a flowing environment. The top images show the movement of the robot in the flowing environment without applying a magnetic field, and the arrow indicates the flowing direction. The bottom images show the propulsion of the robot in a flowing environment with the larva-inspired gait, and the arrow indicates the moving direction of the robot. The scale bar is 5 mm. C) 3D swimming and obstacle-crossing behavior of the robot. The scale bar is 5 mm. D) Crawling inside a narrow tube. The scale bar is 2 mm. E) Series of multimodal locomotion including 2D swimming, immersion, rolling, and 3D swimming. The scale bar is 10 mm.

achieved by the robot. The multimodal locomotion capability makes the robot promising to study the biomechanics of other organisms (such as leech and earthworm) and perform functional tasks in harsh environments.

3. Conclusion and Discussion

In summary, we create a soft robotics-based platform to reconstruct and decouple the complex wiggling motion adopted by midge larvae. The LarvaBot with slender structure can be fabricated by the photopolymerization of magnetic hydrogel material. Through the wireless actuation of programmed magnetic field inputs, the LarvaBot achieves a variety of reprogrammable coupled gaits, including motions that mimic natural larvae locomotion. Furthermore, such a robotic platform provides an enabling technology to systematically decouple the complex wigglings motion generated by larvae and provides insight into how rotation amplitude and the synchronization of curling and rotation can influence propulsion performance. We expect this study could assist in decoupling complex gaits generated by invertebrates and lead to a deeper understanding of their underlying mechanisms. Moreover, it can inform the design and operation of future miniaturized soft robots with programmed swimming gaits that are optimized for enhanced motility.

With further improvement to its material architecture and magnetic operation, the LarvaBot developed in this work could be potentially used for environmental remediation and drug delivery in future direction. By the incorporation of functional agents such as graphene oxide or Ag nanoparticles, the LarvaBot has the potential to execute tasks like the removal of chemical and biological pollution.[59,60] The contact frequency with the contaminant could be increased due to the high motility of the LarvaBot and the hydrogel network infiltrated with water resulting in efficient remediation process. Besides, the robot body could potentially absorb small molecular agents from the medium and deliver them at targeted position by expelling water to fulfill the drug loading and release tasks.[61,62] Several critical issues should be considered before the application of LarvaBot in the real world. First, the impact of the doped materials on the motility of the LarvaBot needs to be evaluated. The proportion of the doped materials should be optimized to achieve optimal performance and motility. Another potential solution is to develop swarm control strategies to improve the efficiency of the task execution.[32,63] Second, the tracking and navigation of the LarvaBot should be investigated systematically to facilitate the in vivo control and precise navigation. The integration with medical imaging systems such as magnetic resonance imaging scanner (MRI) and ultrasound imaging system, and the incorporation of various imaging agents inside the robot body are envisioned to be feasible solution to demonstrate the potential of the robot. For instance, in our recent work, biohybrid magnetic soft robots are deliveried into the bile duct, and the endoscope and ultrasound imaging system are used to the tracking of the delivery process.[32] Meanwhile, the MRI system also has the potential to be used for the actuation of the LarvaBot, since the rotational and translational control of magnetic robots inside the MRI chamber have been successfully realized.[64,65]

4. Experimental Section

Materials: The chemicals of acrylamide (AAm, 99%), polyvinylpyrrolidone (PVP, average $M_\mathrm{w} \approx 1\,300\,000$), glycerol, sodium chloride (NaCl, 99.5%), triethoxy-1H, 1H, 2H, 2H-tridecafluoro-*n*-octylsilane ($C_{14}H_{19}F_{13}O_3Si$, 97%), methylene blue (90.0%), and ammonia solution (25-28%) were obtained from Aladdin Chemicals. *N*,*N*′-methylene bisacrylamide (MBA) was purchased from Beijing Solarbio Science & Technology Co., Ltd. Diphenyl(2,4,6-trimethylbenzoyl) phosphine oxide (TPO-L) was purchased from Shanghai Curease Chemical Co., Ltd. Tetraethylorthosilicate (TEOS) was purchased from J&K Scientific Ltd. NdFeB microparticles with an average size of 5 µm (LW-BA(16-7A)-2000) were purchased from Guangzhou Xinnuode Co., Ltd. All chemicals were used without further purification.

Preparation of PAAm Hydrogel Precursor: First, 2 g AAm, 0.01 g BIS, and 1 g PVP were added to 10 mL deionized water and glycerol mixed solution (mass ratio: 1:1) and then stirred vigorously. After complete dissolution, 200 µL TPO-L/ethanol solution (10 wt%) were mixed, followed by stirring for 10 min.

Preparation of NdFeB@SiO$_2$ Particles: The silica shell of the NdFeB particle was obtained by the hydrolysis and polycondensation of TEOS. First, 18 g NdFeB particles were dispersed in 450 mL ethanol with vigorously stirring, followed by the addition of 27 mL ammonium hydroxide. 1.2 mL TEOS was then slowly added to the mixture. Subsequently, the mixture was stirred for 12 h.

Magnetization Procedure: The internal magnetic domain was programmed by template-assisted magnetization, as shown in Figure 2A. The proposed soft robot was deformed by a rod mold and exposed to a uniform ≈2 T magnetic field produced by a magnetizer. After magnetization, there is a sinusoidal magnetization profile (M) inside the robot body.

Magnetic Actuation Experiments: The soft robot was treated with 1 vol% triethoxy-1H, 1H, 2H, 2H-tridecafluoro-*n*-octylsilane in ethanol to obtain a hydrophobic surface. This treatment could ensure that the robot stably stays on the water surface. A three-axis Helmholtz electromagnetic coil setup was adopted to generate a programmable magnetic field. The proposed dynamic magnetic fields were controlled by custom-programmed software using LabVIEW.

Characterization Techniques: The magnetization profile of the soft robot was measured by a magneto-optical sensor (MagViewS, Matesy, Jena, Germany). The magnetic hysteresis of magnetic particles was measured by a PPMS Model 6000 Quantum Design VSM.

Supporting Information

Supporting Information is available from the Wiley Online Library or from the author.

Acknowledgements

N.X. and B.J. contributed equally to this work. The research work was financially supported by the Hong Kong Research Grants Council with Project No. JLFS/E-402/18, the ITF project with Project No. MRP/036/18X funded by the HKSAR Innovation and Technology Commission (ITC), the Croucher Foundation Grant with Ref. No. CAS20403, the CUHK internal grants, and National Science Foundation of China (NSFC-NSAF Grant No. U1930402). The authors thank the support from Multi-scale Medical Robotics Centre (MRC), InnoHK, at the Hong Kong Science Park, and the SIAT-CUHK Joint Laboratory of Robotics and Intelligent Systems. V.I. acknowledges funding from the European Union's Horizon 2020 research and innovation programme under the Marie Sklodowska-Curie Grant Agreement No. 894425.

Conflict of Interest

The authors declare no conflict of interest.

Data Availability Statement

The data that support the findings of this study are available from the corresponding author upon reasonable request.

Keywords

hydrogel robot, magnetic robotic platform, motion decoupling, wiggling motion

Received: November 11, 2021
Revised: February 6, 2022
Published online: March 18, 2022

[1] M. Burrows, M. Dorosenko, *J. Exp. Biol.* **2014**, *217*, 2468.
[2] Y. Ozkan-Aydin, D. I. Goldman, M. S. Bhamla, *Science* **2021**, *118*, e2010542118.
[3] M. Qin, M. Sun, R. Bai, Y. Mao, X. Qian, D. Sikka, Y. Zhao, H. J. Qi, Z. Suo, X. He, *Adv. Mater.* **2018**, *30*, 1800468.

[4] Z. Ren, W. Hu, X. Dong, M. Sitti, *Nat. Commun.* **2019**, *10*, 2703.
[5] W. Hu, G. Z. Lum, M. Mastrangeli, M. Sitti, *Nature* **2018**, *554*, 81.
[6] Y. Tang, Y. Chi, J. Sun, T.-H. Huang, O. H. Maghsoudi, A. Spence, J. Zhao, H. Su, J. Yin, *Sci. Adv.* **2020**, *6*, eaaz6912.
[7] Y. Ohm, C. Pan, M. J. Ford, X. Huang, J. Liao, C. Majidi, *Nat. Electron.* **2021**, *4*, 185.
[8] X. Liu, C. Steiger, S. Lin, G. A. Parada, J. Liu, H. F. Chan, H. Yuk, N. V. Phan, J. Collins, S. Tamang, *Nat. Commun.* **2019**, *10*, 493.
[9] M. Cianchetti, C. Laschi, A. Menciassi, P. Dario, *Nat. Rev. Mater.* **2018**, *3*, 143.
[10] Y. Wang, X. Yang, Y. Chen, D. K. Wainwright, C. P. Kenaley, Z. Gong, Z. Liu, H. Liu, J. Guan, T. Wang, *Sci. Robot.* **2017**, *2*, eaan8072.
[11] J. M. Rieser, J. L. Tingle, D. I. Goldman, J. R. Mendelson, *Proc. Natl. Acad. Sci. USA* **2021**, 118.
[12] J. A. Nyakatura, K. Melo, T. Horvat, K. Karakasiliotis, V. R. Allen, A. Andikfar, E. Andrada, P. Arnold, J. Lauströer, J. R. Hutchinson, *Nature* **2019**, *565*, 351.
[13] A. J. Ijspeert, *Science* **2014**, *346*, 196.
[14] H. Gu, Q. Boehler, H. Cui, E. Secchi, G. Savorana, C. De Marco, S. Gervasoni, Q. Peyron, T.-Y. Huang, S. Pane, *Nat. Commun.* **2020**, *11*, 2637.
[15] X. Dong, G. Z. Lum, W. Hu, R. Zhang, Z. Ren, P. R. Onck, M. Sitti, *Sci. Adv.* **2020**, *6*, eabc9323.
[16] T. Wang, Z. Ren, W. Hu, M. Li, M. Sitti, *Sci. Adv.* **2021**, *7*, eabf7364.
[17] D. Krishnamurthy, G. Katsikis, A. Bhargava, M. Prakash, *Nat. Phys.* **2017**, *13*, 266.
[18] B. Wang, K. Kostarelos, B. J. Nelson, L. Zhang, *Adv. Mater.* **2020**, *33*, 2002047.
[19] E. W. Hawkes, C. Majidi, M. T. Tolley, *Sci. Robot.* **2021**, *6*, eabg6049.
[20] D. S. Shah, J. P. Powers, L. G. Tilton, S. Kriegman, J. Bongard, R. Kramer-Bottiglio, *Nat. Mach. Intell.* **2021**, *3*, 51.
[21] D. Shah, B. Yang, S. Kriegman, M. Levin, J. Bongard, R. Kramer-Bottiglio, *Adv. Mater.* **2021**, *33*, 2002882.
[22] Y. Kim, H. Yuk, R. Zhao, S. A. Chester, X. Zhao, *Nature* **2018**, *558*, 274.
[23] J. Cui, T.-Y. Huang, Z. Luo, P. Testa, H. Gu, X.-Z. Chen, B. J. Nelson, L. J. Heyderman, *Nature* **2019**, *575*, 164.
[24] Y. Kim, G. A. Parada, S. Liu, X. Zhao, *Sci. Robot.* **2019**, *4*, eaax7329.
[25] X. Hu, I. C. Yasa, Z. Ren, S. R. Goudu, H. Ceylan, W. Hu, M. Sitti, *Sci. Adv.* **2021**, *7*, eabe8436.
[26] J. Zhang, Z. Ren, W. Hu, R. H. Soon, I. C. Yasa, Z. Liu, M. Sitti, *Sci. Robot.* **2021**, *6*, eabf0112.
[27] D. Jin, Q. Chen, T.-Y. Huang, J. Huang, L. Zhang, H. Duan, *Mater. Today* **2020**, *32*, 19.
[28] Y. Zhao, C.-Y. Lo, L. Ruan, C.-H. Pi, C. Kim, Y. Alsaid, I. Frenkel, R. Rico, T.-C. Tsao, X. He, *Sci. Robot.* **2021**, *6*, eabd5483.
[29] X. Liu, Y. Yang, M. E. Inda, S. Lin, J. Wu, Y. Kim, X. Chen, D. Ma, T. K. Lu, X. Zhao, *Adv. Funct. Mater.* **2021**, *31*, 2010918.
[30] J. Yu, B. Wang, X. Du, Q. Wang, L. Zhang, *Nat. Commun.* **2018**, *9*, 3260.
[31] Q. Wang, K. F. Chan, K. Schweizer, X. Du, D. Jin, S. C. H. Yu, B. J. Nelson, L. Zhang, *Sci. Adv.* **2021**, *7*, eabe5914.
[32] B. Wang, K. F. Chan, K. Yuan, Q. Wang, X. Xia, L. Yang, H. Ko, Y.-X. J. Wang, J. J. Y. Sung, P. W. Y. Chiu, *Sci. Robot.* **2021**, *6*, eabd2813.
[33] X. Qian, Y. Zhao, Y. Alsaid, X. Wang, M. Hua, T. Galy, H. Gopalakrishna, Y. Yang, J. Cui, N. Liu, *Nat. Nanotechnol.* **2019**, *14*, 1048.
[34] D. Ahmed, T. Baasch, N. Blondel, N. Läubli, J. Dual, B. J. Nelson, *Nat. Commun.* **2017**, *8*, 770.
[35] Z. Ren, R. Zhang, R. H. Soon, Z. Liu, W. Hu, P. R. Onck, M. Sitti, *Sci. Adv.* **2021**, *7*, eabh2022.
[36] Z. Sun, Y. Yamauchi, F. Araoka, Y. S. Kim, J. Bergueiro, Y. Ishida, Y. Ebina, T. Sasaki, T. Hikima, T. Aida, *Angew. Chem., Int. Ed.* **2018**, *57*, 15772.
[37] X. Huang, K. Kumar, M. K. Jawed, A. M. Nasab, Z. Ye, W. Shan, C. Majidi, *Sci. Robot.* **2018**, *3*, eaau7557.
[38] S. Chen, Y. Cao, M. Sarparast, H. Yuan, L. Dong, X. Tan, C. Cao, *Adv. Mater. Technol.* **2020**, *5*, 1900837.
[39] T. Xu, J. Zhang, M. Salehizadeh, O. Onaizah, E. Diller, *Sci. Robot.* **2019**, *4*, eaav4494.
[40] H. Lu, M. Zhang, Y. Yang, Q. Huang, T. Fukuda, Z. Wang, Y. Shen, *Nat. Commun.* **2018**, *9*, 3944.
[41] J. Brackenbury, *J. Insect Physiol.* **2000**, *46*, 1517.
[42] S. Park, H. Hwang, S.-W. Nam, F. Martinez, R. H. Austin, W. S. Ryu, *PLoS One* **2008**, *3*, e2550.
[43] R. A. Merz, D. R. Edwards, *J. Exp. Mar. Biol. Ecol.* **1998**, *228*, 273.
[44] J. Chen, W. Friesen, T. Iwasaki, *J. Exp. Biol.* **2011**, *214*, 561.
[45] J. Brackenbury, *J. Insect Physiol.* **1999**, *45*, 525.
[46] K. J. Quillin, *J. Exp. Biol.* **1999**, *202*, 661.
[47] S. A. Budick, D. M. O'Malley, *J. Exp. Biol.* **2000**, *203*, 2565.
[48] C. J. Voesenek, F. T. Muijres, J. L. Van Leeuwen, *J. Exp. Biol.* **2018**, *221*, jeb149583.
[49] T. J. Anderson, R. S. Stelzer, H. G. Drecktrah, S. L. Eggert, *Freshwater Sci.* **2012**, *31*, 365.
[50] A. Roskosch, M. R. Morad, A. Khalili, J. Lewandowski, *J. N. Am. Benthol. Soc.* **2010**, *29*, 789.
[51] R. Cornette, O. Gusev, Y. Nakahara, S. Shimura, T. Kikawada, T. Okuda, *Zool. Sci.* **2015**, *32*, 248.
[52] J. Brackenbury, *J. Zool.* **2003**, *260*, 195.
[53] G. I. Taylor, *Proc. Math. Phys. Eng. Sci.* **1952**, *214*, 158.
[54] H.-W. Huang, F. E. Uslu, P. Katsamba, E. Lauga, M. S. Sakar, B. J. Nelson, *Sci. Adv.* **2019**, *5*, eaau1532.
[55] J. Zhang, E. Diller, *Soft Robot* **2018**, *5*, 761.
[56] S. Wu, Q. Ze, R. Zhang, N. Hu, Y. Cheng, F. Yang, R. Zhao, *ACS Appl. Mater. Interfaces* **2019**, *11*, 41649.
[57] Y. Zhao, C. Xuan, X. Qian, Y. Alsaid, M. Hua, L. Jin, X. He, *Sci. Robot.* **2019**, *4*, eaax7112.
[58] L. A. Smock, *Freshwater Biol.* **1980**, *10*, 375.
[59] Y. Dong, L. Wang, J. Wang, S. Wang, Y. Wang, D. Jin, P. Chen, W. Du, L. Zhang, B. F. Liu, *ACS Nano* **2020**, *14*, 16600.
[60] X. Liu, J. Liu, S. Lin, X. Zhao, *Mater. Today* **2020**, *36*, 102.
[61] H. Bodugoz-Senturk, C. E. Macias, J. H. Kung, O. K. Muratoglu, *Biomaterials* **2009**, *30*, 589.
[62] D. Jin, K. Yuan, X. Du, Q. Wang, S. Wang, L. Zhang, *Adv. Mater.* **2021**, *33*, 2100070.
[63] S. Won, S. Kim, J. E. Park, J. Jeon, J. J. Wie, *Nat. Commun.* **2019**, *10*, 4751.
[64] O. Erin, M. Boyvat, J. Lazovic, M. E. Tiryaki, M. Sitti, *Adv. Sci.* **2021**, *8*, 2100463.
[65] O. Erin, H. B. Gilbert, A. F. Tabak, M. Sitti, *IEEE Trans. Robot.* **2019**, *35*, 1323.